




Article

Thermal Stability and Radiation Tolerance of Lanthanide-Doped Cerium Oxide Nanocubes

Kory Burns ^{1,2}, Paris C. Reuel ³, Fernando Guerrero ³, Eric Lang ¹, Ping Lu ¹, Assel Aitkaliyeva ² , Khalid Hattar ^{1,*}  and Timothy J. Boyle ^{3,*} 

¹ Center for Integrated Nanotechnologies, Sandia National Laboratories, P.O. Box 8500, Albuquerque, NM 87185, USA; kdburns@sandia.gov (K.B.); ejlang@sandia.gov (E.L.); plu@sandia.gov (P.L.)

² Department of Materials Science and Engineering, University of Florida, Gainesville, FL 32611, USA; aitkaliyeva@mse.ufl.edu

³ Advanced Materials Laboratory, Sandia National Laboratories, Albuquerque, NM 87106, USA; preuel@sandia.gov (P.C.R.); 2guerrero2@gmail.com (F.G.)

* Correspondence: khattar@sandia.gov (K.H.); tjboyle@sandia.gov (T.J.B.); Tel.: +1-(505)-272-7625 (T.J.B.)

Abstract: The thermal and radiation stability of free-standing ceramic nanoparticles that are under consideration as potential fillers for the improved thermal and radiation stability of polymeric matrices were investigated by a set of transmission electron microscopy (TEM) studies. A series of lanthanide-doped ceria (Ln:CeO_x; Ln = Nd, Er, Eu, Lu) nanocubes/nanoparticles was characterized as synthesized prior to inclusion into the polymers. The Ln:CeO_x were synthesized from different solution precipitation (oleylamine (ON), hexamethylenetetramine (HMTA) and solvothermal (*t*-butylamine (TBA)) routes. The dopants were selected to explore the impact that the cation has on the final properties of the resultant nanoparticles. The baseline CeO_x and the subsequent Ln:CeO_x particles were isolated as: (i) ON-Ce (not applicable), Nd (34.2 nm), Er (27.8 nm), Eu (42.4 nm), and Lu (287.4 nm); (ii) HMTA-Ce (5.8 nm), Nd (6.6 nm), Er (370.0 nm), Eu (340.6 nm), and Lu (287.4 nm); and (iii) TBA-Ce (4.1 nm), Nd (5.0 nm), Er (3.8 nm), Eu (7.3 nm), and Lu (3.8 nm). The resulting Ln:CeO_x nanomaterials were characterized using a variety of analytical tools, including: X-ray fluorescence (XRF), powder X-ray diffraction (pXRD), TEM with selected area electron diffraction (SAED), and energy dispersive X-ray spectroscopy (EDS) for nanoscale elemental mapping. From these samples, the Eu:CeO_x (ON, HMTA, and TBA) series were selected for stability studies due to the uniformity of the nanocubes. Through the focus on the nanoparticle properties, the thermal and radiation stability of these nanocubes were determined through in situ TEM heating and ex situ TEM irradiation. These results were coupled with data analysis to calculate the changes in size and aerial density. The particles were generally found to exhibit strong thermal stability but underwent amorphization as a result of heavy ion irradiation at high fluences.

Keywords: nanoparticles; in situ TEM; ion irradiation; thermal annealing; ceria



Citation: Burns, K.; Reuel, P.C.; Guerrero, F.; Lang, E.; Lu, P.; Aitkaliyeva, A.; Hattar, K.; Boyle, T.J. Thermal Stability and Radiation Tolerance of Lanthanide-Doped Cerium Oxide Nanocubes. *Crystals* **2021**, *11*, 1369. <https://doi.org/10.3390/cryst11111369>

Academic Editors:
Alessandra Toncelli and Željka Antić

Received: 1 October 2021
Accepted: 5 November 2021
Published: 11 November 2021

Publisher's Note: MDPI stays neutral with regard to jurisdictional claims in published maps and institutional affiliations.



Copyright: © 2021 by the authors. Licensee MDPI, Basel, Switzerland. This article is an open access article distributed under the terms and conditions of the Creative Commons Attribution (CC BY) license (<https://creativecommons.org/licenses/by/4.0/>).

1. Introduction

Lanthanum oxide (LnO_x) nanomaterials are of interest as potential fillers in polymeric coatings to protect internal electronic components and circuits from high temperature and ionization exposure (i.e., rad-hard). This is mainly due to their high Z number, which helps to prevent the ionization of energy and variable oxidation state, which can be accessed when exposed to ionizing radiation-reducing Compton and Auger effects [1]. Computational studies using WinXCom software indicate that g-photons (1 keV–100 GeV) interacting with LnO_x (Ln=La, Ce, Pr, Nd, Eu, Dy, Sm, Er, Yb, Lu) are effective shielding agents [2,3]. A number of systems have demonstrated their utility, such as LnO_x (La [4], Ce, Nd, Sm)-doped borate glasses, which were found to effect γ-ray shielding [5]. To overcome the brittle nature of the ceramic oxide materials, the development of composite coatings (polymers with LnO_x nanofillers) allows for a flexible, stable layer that is also rad-hard.

While proving to be an effective shielding agent against electromagnetic radiation, ceria (CeO_2) has been shown to be very sensitive to ion irradiation [6]. In ion-matter interaction theory, an impinging ion penetrates a target material and transfers its energy by both elastic and inelastic collisions with the target nuclei and target electrons, respectively. In previous reports, high doses of 2 MeV Au ion irradiation produced significant disorder on the Ce sub-lattice caused by inelastic collisions [6]. This is in direct contrast to 2.5 MeV electron beam irradiations, where elastic collisions produced isolated defects that were easily repaired by thermal annealing [7]. This suggests that dopant atoms within CeO_2 may be warranted to enhance radiation stability and prevent significant lattice disorder upon interaction with external stimuli. There are several candidate Ln dopants that have shown promise when utilized in electronic components from high radiation environments, in part due to their high threshold energies [8]. The Ln cations discussed in this report were selected due to their availability, representation across the Ln series, diverse oxidation states available, and diverse applications: EuO_x is used as an activation ion for color television phosphor, ErO_x is used as a gate dielectric in CMOS logic circuits in space environments, NdO_x is used as a ceramic capacitor, and LuO_x is used as a laser crystal for solid-state lasers [3].

For this work, we were interested in exploiting ceria (CeO_x) beyond the wide range of applications for which it is already used [9,10], including: catalysts [11,12], biomedical applications [1,12–14], actinide surrogates [15], pigments [16], sunscreen [12,13,17], and many other applications, as well as less frequently investigated rad-hard coatings. As mentioned above, studies have shown that doping Ln cations into the lattice of CeO_x nanoparticles imparts changes to their final properties, including improved radiative recombination, reduced oxidation catalytic activity, enhanced UV-absorption capacity, and the promotion of intermediate electronic levels in the bandgap [12,14,17,18]. Herein, a study of lanthanide doped- CeO_x ($\text{Ln}:\text{CeO}_x$) nanomaterials was undertaken to evaluate the thermal and radiation stability of the nanoparticles through in situ Transmission Electron Microscopy (TEM) techniques [19].

In an effort to explore the properties of $\text{Ln}:\text{CeO}_x$ nanoparticles, a series of nanoparticles was generated using oleylamine (ON) [20], hexamethylenetetramine (HMTA) [21], and *t*-butylamine (TBA) [22] as surfactants. The lanthanide cations used for dopants included Nd, Eu, Er, and Lu, which were selected to represent the series and are well known to occupy alternative oxidation states. The doping was verified by Scanning Transmission Electron Microscopy (STEM)-based EDS elemental mapping. The structural evolution from annealing and irradiation was verified using the unique in situ ion irradiation TEM (I^3TEM) available at Sandia National Laboratories. The results of the synthesis route, ligand, dopant, and resulting particulates were evaluated.

2. Experimental

Nanoparticle preparations were conducted on the bench-top under ambient atmospheric conditions using chemicals obtained and used as received from Aldrich Chemical Company, Inc. (Milwaukee, WI, USA). The lanthanide chloride hydrates ($[\text{LnCl}_3 \cdot 6\text{H}_2\text{O}]$) and nitrates ($[\text{Ln}(\text{NO}_3)_3 \cdot 6\text{H}_2\text{O}]$) were synthesized in-house using the appropriate metal and concentrated acid ((aq) HCl or (aq) HNO_3). All of the Ln precursors structures were verified by single-crystal X-ray experiments. Three routes to nanocubes or nanorods were evaluated, with modifications noted below: (i) oleylamine (ON) [17], (ii) hexamethylenetetramine (HMTA) [18], or (iii) *t*-butylamine (TBA) [19]. All the generated nanoparticle samples (ON, HMTA, TBA) were characterized by a variety of analytical methods: X-ray Fluorescence (XRF), Powder X-ray Diffraction (pXRD), Fourier Transformed InfraRed Spectroscopy (FTIR), and Dynamic Light Scattering (DLS). Full details of the instrumentation and product characterization are available in the Supplementary Materials. General descriptions of the three different routes to CeO_2 and $\text{Ln}:\text{CeO}_x$, where Ln = Eu, Er, and Lu are presented below. The yields were not determined due to the presence of excess surfactants. A summary of the analytical characterization can be found in Table 1.

Table 1. Summarized results of XRF, pXRD, ATR-FTIR, and DLS for CeO₂, Nd:CeO₂, Eu:CeO₂, Er:CeO₂, and Lu:CeO₂. The ATR-FTIR spectrum bends and stretches are further noted with medium (m), strong (s), weak (w), broad (br). Graphical representations of the data shown can be found in the Supplementary Materials.

	CeO ₂	Nd:CeO _x	Eu:CeO _x	Er:CeO _x	Lu:CeO _x
XRF	Ce (major) Eu (minor) Cl(minor)	Ce (major) Nd (minor) Cl (minor) Zr (minor)	Ce (major) Eu (minor) Cl (minor)	Ce (major) Er (minor)	Ce (major) Lu (minor)
pXRD	(25 °C) PDF 00-067-0123 CeO ₂ ceria Cerium Oxide	(600 °C) PDF 00-067-0123 CeO ₂ ceria Cerium Oxide	(600 °C) PDF 00-067-0122 CeO ₂ ceria Cerium Oxide	(600 °C) PDF 00-067-0123 CeO ₂ ceria Cerium Oxide	(600 °C) PDF 00-067-0123 CeO ₂ ceria Cerium Oxide
ATR-FTIR (cm⁻¹)		3355.01 (m, br) 2923.12 (m) 2853.10 (m) 2583.18 (w) 2164.12 (w) 2079.88 (w) 1980.97 (w) 1467.17 (s) 1393.84 (s) 1260.87 (w) 1083.29 (w) 843.62 (m) 802.36 (m) 708.90 (m)	3340.37 (m) 3003.64 (w) 2920.74 (s) 2851.20 (m) 2162.81 (w) 2035.73 (w) 1494.59 (m) 1460.04 (s) 1404.08 (m) 1079.23 (w) 965.75 (w) 841.10 (w) 720.57 (m)	3323.03 (s) 3213.14 (s) 2920.59 (s) 2851.22 (m) 2214.27 (w) 1624.61 (s) 1462.78 (w) 1410.58 (m) 1049.92 (w) 966.31 (w) 719.16 (s)	3315.26 (s) 3210.01 (s) 2922.62 (m) 2852.34 (w) 2216.86 (w) 1618.16 (s) 1411.97 (m) 1117.11 (w) 966.47 (w) 699.03 (m)
DLS (nm)	257 (100%)	295 (100%)	257 (54%) 901 (46%)	343 (100%)	518 (100%)

X-ray Fluorescence (XRF). A ThermoFisher ARL (West Palm Beach, FL, USA) Quant'X EDXRF, DLS Spectrometer utilizing UniQuant software was used for all the analyses. The system uses a Fundamental Parameters approach based on the Sherman equation for the direct measurement of elemental concentrations based on integrated fluorescent peak intensities. In air, using a medium count rate, a single-repetition, multi-scan excitation (C Thin (5 kV, 60 s); Al (12 kV, 100 s), Pd Thick (28 kV, 100 s); Cu Thick (50 kV, 100 s)) was used to evaluate each sample.

Powder X-ray Diffraction (pXRD). The powders were collected on a Bruker D8 Avance diffractometer employing Cu K_α radiation (1.5406 Å) and a RTMS X'Celerator detector. The data were collected over a 2θ range of 5–70° at a scan rate of 0.083°/s and a zero-background holder was employed. The XRD patterns were analyzed using Bruker EVA software and indexed using the Powder Diffraction File PDF-4 + 2013.

Fourier Transformed InfraRed Spectroscopy (FTIR). The FTIR spectral data were collected on a Bruker Vector 22 MIR Spectrometer in an atmosphere of flowing nitrogen using an ATR powder attachment.

Dynamic Light Scattering (DLS). The DLS data were collected on a Malvern Instruments Zetasizer Nanoseries (NanoZS). All the samples were dispersed by sonication for 10 min at 50–60 Hz in their respective solvents (ON–methanol, Parr–tol, HMTA–water). Following the sonication, the samples were diluted and loaded into 1 cm glass cuvettes. A total of 10 sets of scans was performed for each sample to generate an average size distribution by intensity.

- Oleylamine (ON) [17]. In a round-bottomed flask, (CeCl₃•6H₂O) and any dopant (LnCl₃•6H₂O) where Ln = Nd, Eu, Er, and Lu were added to ON. After heating the

reaction to 90 °C and stirring for 1 h, the reaction was then warmed to 265 °C. The reaction turned from pale brown to black. After cooling to room temperature, the solution was collected by centrifugation, washed with ethanol and hexanes and used without further manipulations.

- Hexamethylenetetramine (HMTA) [18]. In a round-bottomed flask, $(\text{Ce}(\text{NO}_3)_3 \cdot 6\text{H}_2\text{O})$ and any dopant $(\text{Ln}(\text{NO}_3)_3 \cdot 6\text{H}_2\text{O})$ where $\text{Ln} = \text{Nd}, \text{Eu}, \text{Er}, \text{and Lu}$ were dissolved in water. An equal volume of concentrated HMTA was added at room temperature and the reaction was allowed to stir (24 h). The precipitate was collected by centrifugation, washed with hexanes and used without further manipulations.
- *t*-butylamine (TBA) [19]. In an Ehrlyenmeyer flask, $(\text{Ce}(\text{NO}_3)_3 \cdot 6\text{H}_2\text{O})$ and any dopant $(\text{Ln}(\text{NO}_3)_3 \cdot 6\text{H}_2\text{O})$ where $\text{Ln} = \text{Nd}, \text{Eu}, \text{Er}, \text{and Lu}$ were dissolved in water and poured into a TeflonTM-lined Parr-bombTM. To this mixture, toluene, oleic acid, and *t*-butylamine were added; the sample was sealed and heated at 180 °C for 12 h. The precipitate was collected by centrifugation, washed with hexanes, and used without further manipulations.

Transmission Electron Microscopy (TEM). The TEM samples were prepared by making a slurry of the powders isolated (vide supra) in methanol, sonicating them for 10 min at 50–60 Hz, and then dropping one drop of solution onto a lacey carbon TEM grid and allow for the solution to volatilize.

The TEM micrographs and selected area electron diffraction (SAED) patterns were collected using a highly modified JEOL 2100 TEM operating at an accelerating voltage of 200 keV. A FEI TitanTM G2 80–200 STEM with a Cs probe corrector and ChemiSTEMTM technology (X-FEGTM and SuperXTM EDS with four windowless silicon drift detectors) operated at 200 kV was used for compositional and structural analysis using EDS spectral imaging and high-angle annular dark-field (HAADF) imaging. The EDS spectral imaging was acquired as a series of frames, where the same region was scanned multiple times with a total acquisition time of over 30 min. An electron probe of size of about 0.13 nm, with a convergence angle of 18.1 mrad, and a current of ~75 pA was used for the EDS acquisition. The Ce L lines and Eu L lines were used for constructing the EDS maps of Ce and Eu, respectively. Since the Ce L lines overlap with the Eu L lines significantly, the EDS spectra were deconvoluted pixel-by-pixel using pure spectra of Ce and Eu as references before map construction. The HAADF images were recorded under similar optical conditions using an annular detector with a collection range of 60–160 mrad. The thermal anneals were performed utilizing the Gatan Heating stage in a JEOL 2100 up to 500 °C.

Heavy Ion Irradiation. The ex situ ion irradiations were performed on previously prepared TEM samples for the powders listed from the preparation routes noted above. The specimens were subjected to 15 MeV Au^{4+} ion irradiation at room temperature using a 6 MV HVEE EN tandem accelerator. The ion fluence range included 1×10^{13} and $1 \times 10^{15} \text{ cm}^{-2}$.

3. Results and Discussion

The interest in the addition of $\text{Ln}:\text{CeO}_x$ nanomaterial into polymers as a means through which to improve their properties (thermal and radiation tolerance) led us to prepare and characterize the particles prior to more complex studies. The dopants (none, Nd, Eu, Er, Lu) were selected to explore the size and electronic impact on the final behavior of the resulting $\text{Ln}:\text{CeO}_x$. Three selected paths focused on synthesis routes that could produce morphologically varied particles, involving different processing parameters, amenability processing for scale up, and different amine surfactants. Details concerning the: Section 3.1. Synthesis and Characterization of the nanoparticles, Section 3.2. Dopant Mapping for Eu, Section 3.3. Thermal Stability, and Section 3.4. Radiation Stability are presented sequentially in the sections below.

3.1. Synthesis and Characterization

The synthesis of nanoparticles following three routes (ON [17], HMTA [18], and TBA [19]) were undertaken as described in the Section 2, with full details available in the Supplementary Materials. The results of the syntheses are presented, followed by in situ and ex situ TEM thermal and ion irradiation measurements, respectively.

Oleylamine (ON). For the ON preparation, the resulting precipitates were independently collected by centrifugation. The green (unprocessed), undoped Ce particles were found to be CeO_2 by pXRD patterns. For the dopants, initial efforts focused on whether the dopant had precipitated with, or within, the CeO_x matrix. The XRF analysis confirmed the presence of each of the different cations (Nd, Eu, Er, and Lu). However, there was also a trace amount of Cl that was associated with the starting precursor ligands. Noted in the Nd: CeO_x (ON) sample was the presence of Zr, which was attributed to a mis-assignment or external contamination. The pXRD patterns of the doped species were in agreement with several different phases of CeO_x along with numerous, minor unidentified peaks which were attributed to the organic surfactants. This assignment proved valid when the samples were thermally treated and the lower ‘organic’ peaks were lost and phase pure CeO_2 was identified. The FTIR analyses of all these samples verified that ON was present on each sample. Further analysis of the particulates available in solution were determined by the DLS measurements. For these samples, the particles were found to range from 257–518 nm in size. The larger size noted for the Eu dopant was attributed to the clustering of the smaller particles in solution. In order to assess the size of the crystallites formed, a TEM analysis was undertaken. For the undoped species, a polymeric matrix was found to surround the particles. The source of this is not known at this time, but its presence made high-resolution identification (bright field imaging and SAED) of the final particles difficult. Nonetheless, fine particles in the order of ~1–2 nm in diameter were observed. By contrast, the doped- CeO_x specimens were found to have formed nanocubes that were ~30 nm in dimension. Further, these particles were found to be highly crystalline, as determined by the SAED analyses.

Hexamethylenetetramine (HMTA). Similarly, the XRF of HMTA showed each powder had the proper Ln cations present. The pXRD patterns of the green undoped Ce as well as the doped Nd matched the phase pure CeO_2 . For the rest of the Ln: CeO_x (HMTA) samples, again, a number of different phases of cerium oxide with minor HMTA species were present. Similarly, heat treatment produced phase pure CeO_2 and the loss of the ‘organic’ peaks. The FTIR clearly showed HMTA present on each of the samples. The DLS analyses showed a wide range of particles available from 33–463 nm. Again, Eu displayed two different sizes of particulate. The TEM analysis confirmed the small (~2–6 nm) octahedral-shaped particles for the undoped species, while the doped particles featured similarly shaped species, with sizes ranging from 80–200 nm.

t-butylamine (TBA). The substantially smaller amount of material made available by the Parr bomb approach using TBA made characterization much more difficult. However, for each sample, XRF showed the proper cations were present and that most phases were CeO_2 with Lu having an additional carbonate phase. For each, similar FTIR data were compiled and were consistent with the TBA and the other species that were used in the reduction of the nitrate precursor. The DLS data were very consistent in comparison, ranging only from 23–68 nm in size, with both Nd and Er demonstrating some cluster formation (222 and 424 nm, respectively). TEM analysis showed crystallite samples that were in the order of ~2–7 nm in size for the doped and undoped species.

For each of these routes, the nanoparticles were isolated, with only a few featuring residual starting ligands. The pXRD patterns revealed that organic moieties that were consistent with the various surfactants (ON, HMTA, TBA) for the different processes. The heat treatment of the samples led to the formation of phase pure CeO_2 . The DLS showed much larger particles were present, but this was attributed to clustering. The crystal size was confirmed to be nanoparticles by the TEM analysis for each sample, as shown in Figure 1: (i) ON-Ce (not applicable), Nd (34.2 nm), Er (27.8 nm), Eu (42.4 nm), Lu

(287.4 nm); (ii) HMTA-Ce (5.8 nm), Nd (6.6 nm), Er (370.0 nm), Eu (340.6 nm), Lu (287.4 nm); and (iii) TBA-Ce (4.1 nm), Nd (5.0 nm), Er (3.8 nm), Eu (7.3 nm), Lu (3.8 nm). The ON all appeared to be below 50 nm in size and formed cubes, except for the Lu species, which were an order of magnitude larger in size. In comparison, the HMTA particles were similar for Ce and Nd (~5–6 nm) but the other doped species were again an order of magnitude larger. Further, these particles were irregular round species. Finally, the TBA nanocubes all proved to be <8 nm.

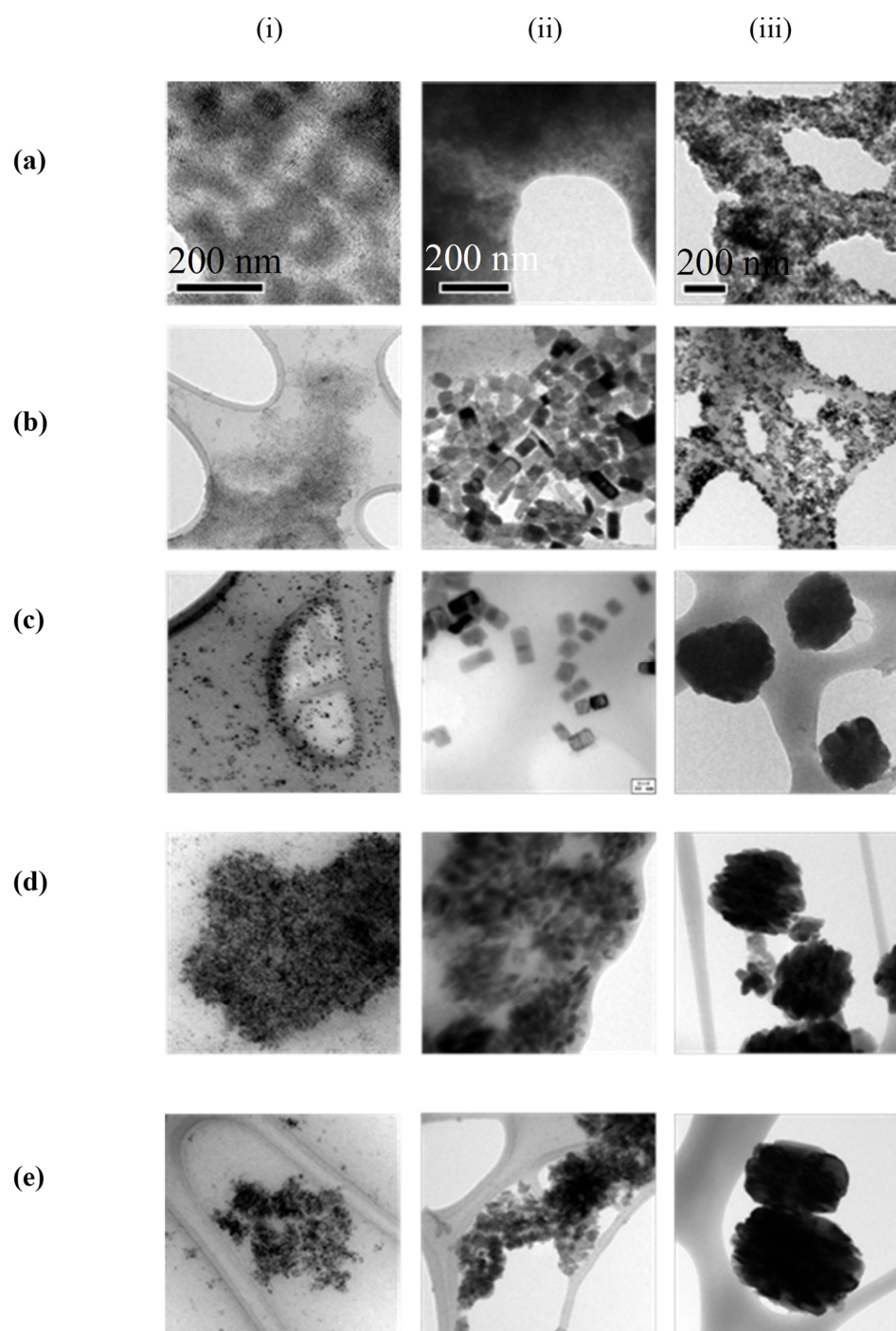


Figure 1. TEM images of column (i) TBA, (ii) ON, and (iii) HMTA-generated nanoparticles of column (a) CeO_x, (b) Nd:CeO_x, (c) Eu:CeO_x, (d) Er:CeO_x, and (e) Lu:CeO_x.

The samples were analyzed by XRF, which confirmed that the various dopants and Ce were present. In some instances, minor residual cations were observed, but in general, the cations introduced were isolated in the precipitate. The pXRD patterns confirmed for all the samples that CeO_2 was formed, with no indication of minor dopant oxide phases. This implies that the Ln dopants were successfully incorporated into the CeO_2 lattice. TEM elemental mapping was used to verify this concept (*vide infra*). The FTIR data revealed the presence of the various surfactants (HDA, ON, and TBA) on the isolated particles. It is difficult to distinguish between bound and free ligands, but it is believed that after extensive washing, the remaining bends and shifts are associated with the bound surfactants. DLS data revealed that sub-micron species were present in solution, which is consistent with the TEM data collected (*vide infra*). See Table 1 for a summary of the various results obtained on each sample and Supplementary Materials for the raw data.

3.2. Dopant Mapping for Eu

Based on the TEM images of the dopants across the different preparation routes, the variability in their oxidation states and their more centric sizes, the Eu: CeO_x samples were selected for further study by HAADF imaging and EDS mapping (ON, HMTA, and TBA in Figures 2–4, respectively). While the above data (see Table 1) confirm the presence of the desired Eu dopant, its size, and its initial phase assignments, it was critical to verify the that Eu dopant was within the CeO_x matrix; thus, elemental mapping was undertaken.

For the ON sample, the $\text{CeO}_x(\text{ON})$ exhibited a much finer particle size (<2 nm; Figure 2a) than the doped Eu: $\text{CeO}_x(\text{ON})$ samples (20–50 nm; Figure 2b). The EDS mapping for the Eu: $\text{CeO}_x(\text{ON})$ species verified that the Eu-dopant was present within the CeO_x matrix (Figure 2c). Notably, several minor contaminants were identified that were not involved in the synthesis, such as a Si-based polymeric matrix. Additionally, Cl particles consistent with the XRF studies were found within the particles that most likely originated from the starting precursors. As shown in Figure 3, the $\text{CeO}_x(\text{HMTA})$ particles were found to feature an average size of ~4 nm, whereas the Eu: $\text{CeO}_x(\text{HMTA})$ were found to be considerably larger (~300 nm). The EDS mapping showed the uniform distribution of Eu within the large Eu: $\text{CeO}_x(\text{HMTA})$ particles (Figure 3c). As in the Eu: $\text{CeO}_x(\text{ON})$, Cl contamination was observed, along with other smaller impurities (Fe and Si), the presence of which is unaccounted for as they were not used in the part of the synthesis; however, as these elements were not identified by the XRF studies, it is believed an external contamination source may have accounted for their presence. The $\text{CeO}_x(\text{TBA})$ and Eu: $\text{CeO}_x(\text{TBA})$ samples were determined to be cubes 2–5 nm in size (Figure 4a,b) and the distribution of Eu within the Eu: CeO_x was verified by the EDS maps (Figure 4c).

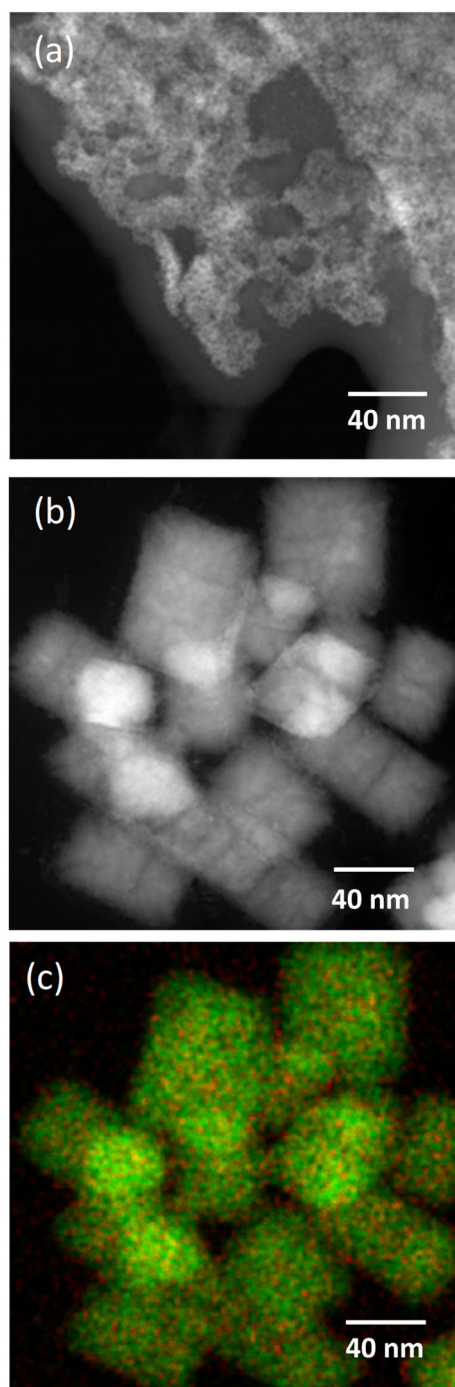


Figure 2. STEM HAADF imaging and EDS mapping of nanoparticles generated by ON: (a) HAADF of CeO_x and (b) HAADF of Eu:CeO_x ; (c) Ce and Eu L map of the Eu:CeO_x NPs (Eu L—red, Ce—green).

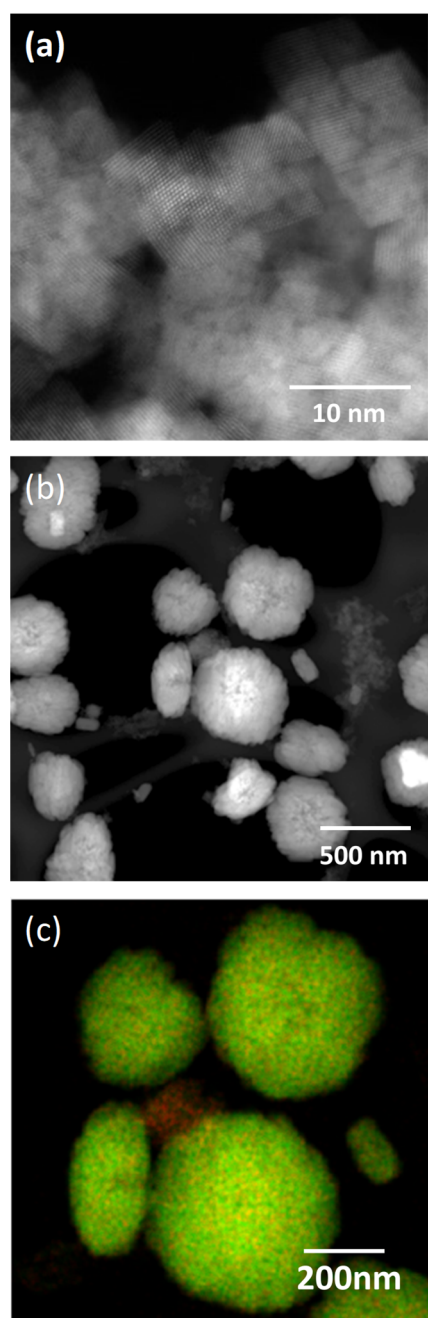


Figure 3. STEM HAADF imaging and EDS mapping of nanoparticles generated by HMTA: (a) HAADF of CeO_x and (b) HAADF of Eu:CeO_x ; (c) Ce and Eu L map of the Eu:CeO_x NPs (Eu L—red, Ce L—green).

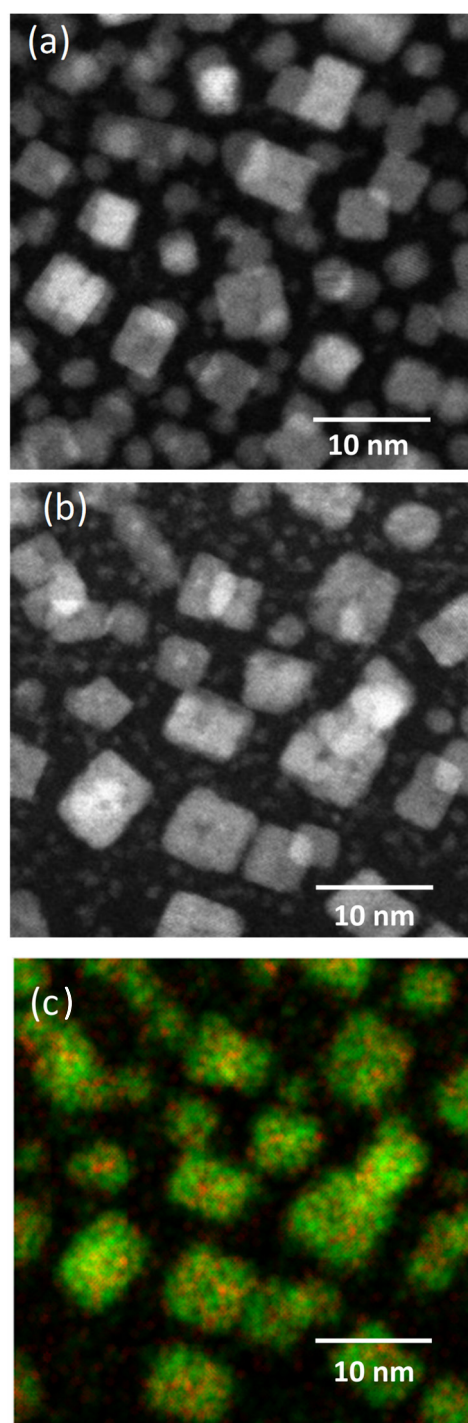


Figure 4. STEM HAADF imaging and EDS mapping of nanoparticles generated by TBA: (a) HAADF of CeO_x and (b) HAADF of Eu:CeO_x ; (c) Ce L and Eu L map of the Eu:CeO_x NPs (Eu L—red, CeL—green).

3.3. Thermal Stability

In situ thermal annealing experiments were carried out on all the samples (ON, HMTA, TBA), as shown in Figures 5–7, respectively. Each specimen was heated from room temperature to 500 °C at an average heating rate of 0.5 °C/s. For the ON specimens ($\text{CeO}_x(\text{ON})$; Figure 5), the samples proved to be unstable under the electron beam, which was attributed to a high impurity concentration and the formation of complex oxides during the preparation route. This was emphasized further during annealing, and it was

not possible to perform a statistical analysis. Further, the $\text{Eu:CeO}_x(\text{ON})$ sample displayed an initial increase in areal density, followed by a decrease from 100–200 °C. In this temperature regime, sputtering dominated the response of the material, which was likely due to an increase in momentum exchange between the atoms in the solid, which was accelerated by an increase in temperature, and thus an increase in mobility. The $\text{CeO}_x(\text{HMTA})$ samples were found to be mainly glommed together over the grid; nonetheless, well separated nanoparticles were observed in several areas, and these sections were used for thermal investigation. Upon heating, the nanoparticles that were in the highly concentrated regions were found to ‘de-cluster’, which was attributed to the thermal-induced mobility. It was also noted that the overall size of the nanoparticle material increased through the heating experiment. This was not due to sintering but, instead, to the emergence of larger nanoparticles from the room temperature cluster areas.

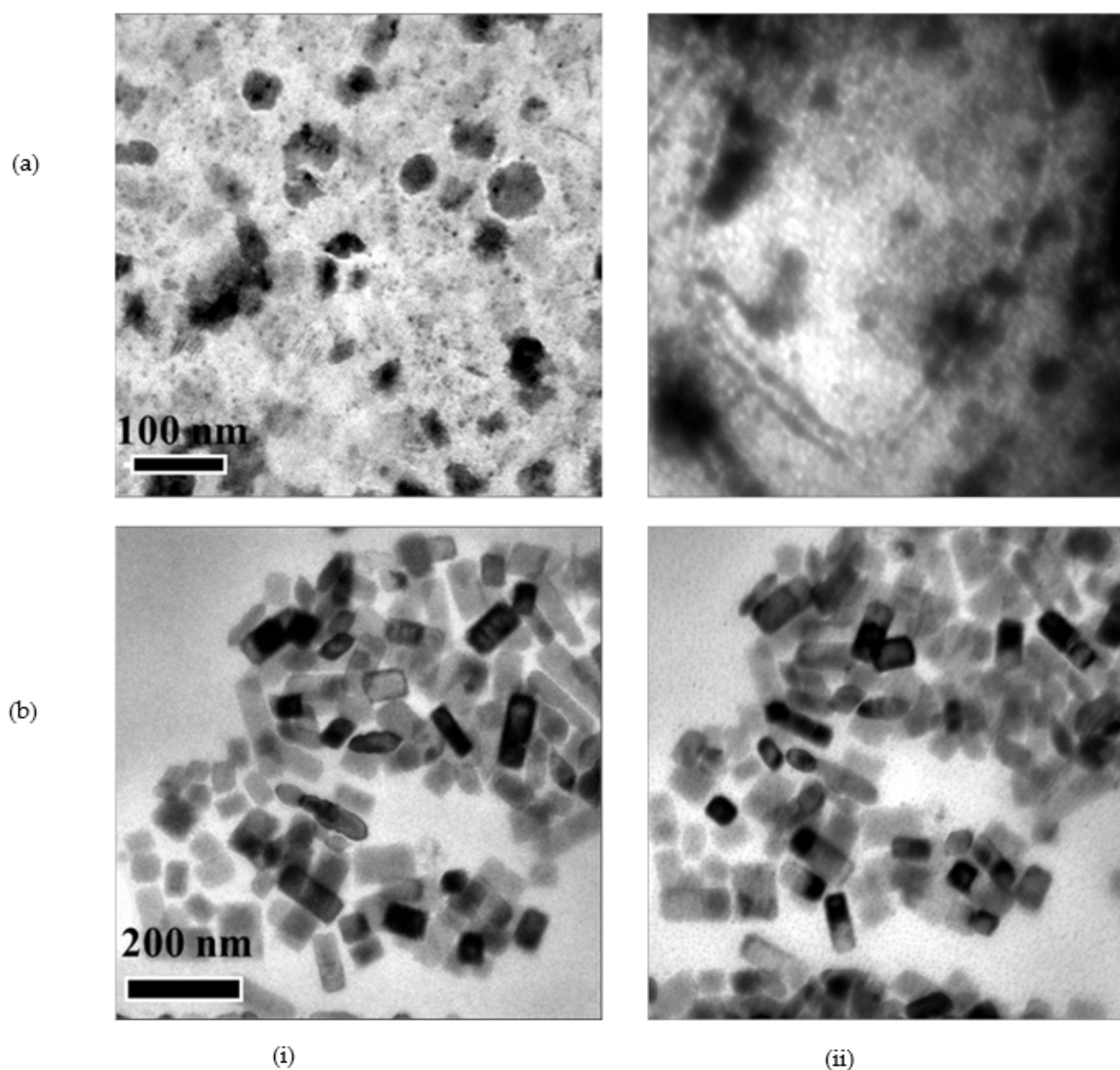


Figure 5. TEM images of nanoparticles generated from ON preparation route during thermal annealing: (i) 25 °C and (ii) 500 °C where (a) CeO_x (scale bar = 100 nm) and (b) Eu:CeO_x (scale bar = 200 nm).

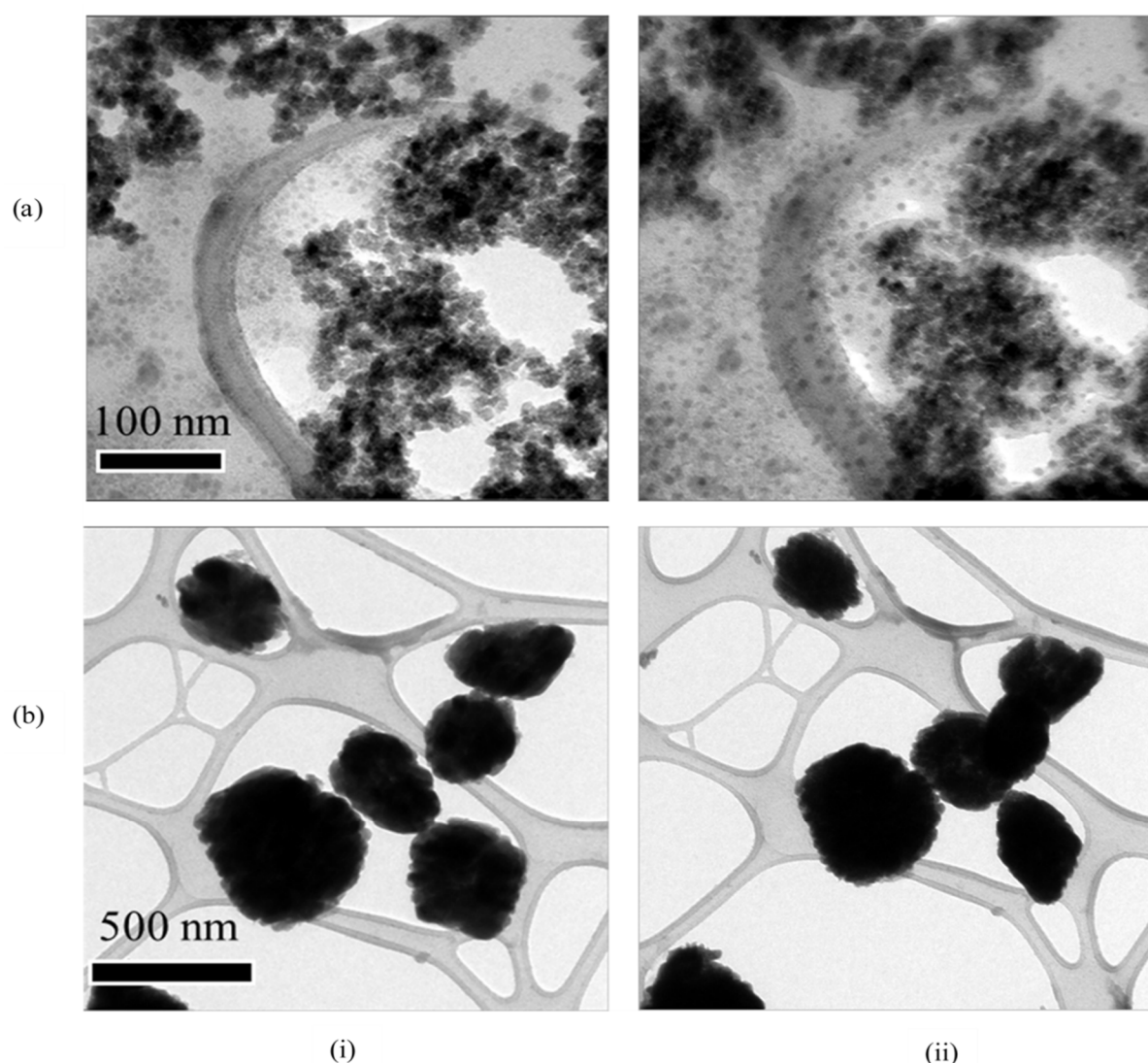


Figure 6. TEM images of nanoparticles generated from HMTA preparation route during thermal annealing: (i) 25 °C and (ii) 500 °C where (a) CeO_x (scale bar = 100 nm) and (b) Eu:CeO_x (scale bar = 500 nm).

The sizes of the $\text{Eu:CeO}_x(\text{HMTA})$ were unchanged over the temperature range investigated; however, the distance between the particles decreased as the organic ligands were thermally decomposed, allowing in situ clustering. Finally, the $\text{CeO}_x(\text{TBA})$ particles, analyzed in the same fashion, displayed the highest areal density of any particle studied coupled with the smallest average size. These nanoparticles showed a relatively low mobility under annealing conditions but still agglomerated at higher temperatures. For the $\text{Eu:CeO}_x(\text{TBA})$ samples, the particles appeared to destabilize at 200–300 °C, as suggested by the reduced areal density in comparison to the room temperature value. Table 2 provides a summary of the results from the thermal annealing experiments. In order to compare the various changes induced by the thermal study, the sizes of the samples were normalized and a plot of these versus the temperature was generated. As can be seen in Table 2, the Eu:CeO_x nanocubes appeared to be more resistant to deformation compared to the CeO_x samples. This implies that Ln dopants may be modulating the thermal resistance of nanocubes.

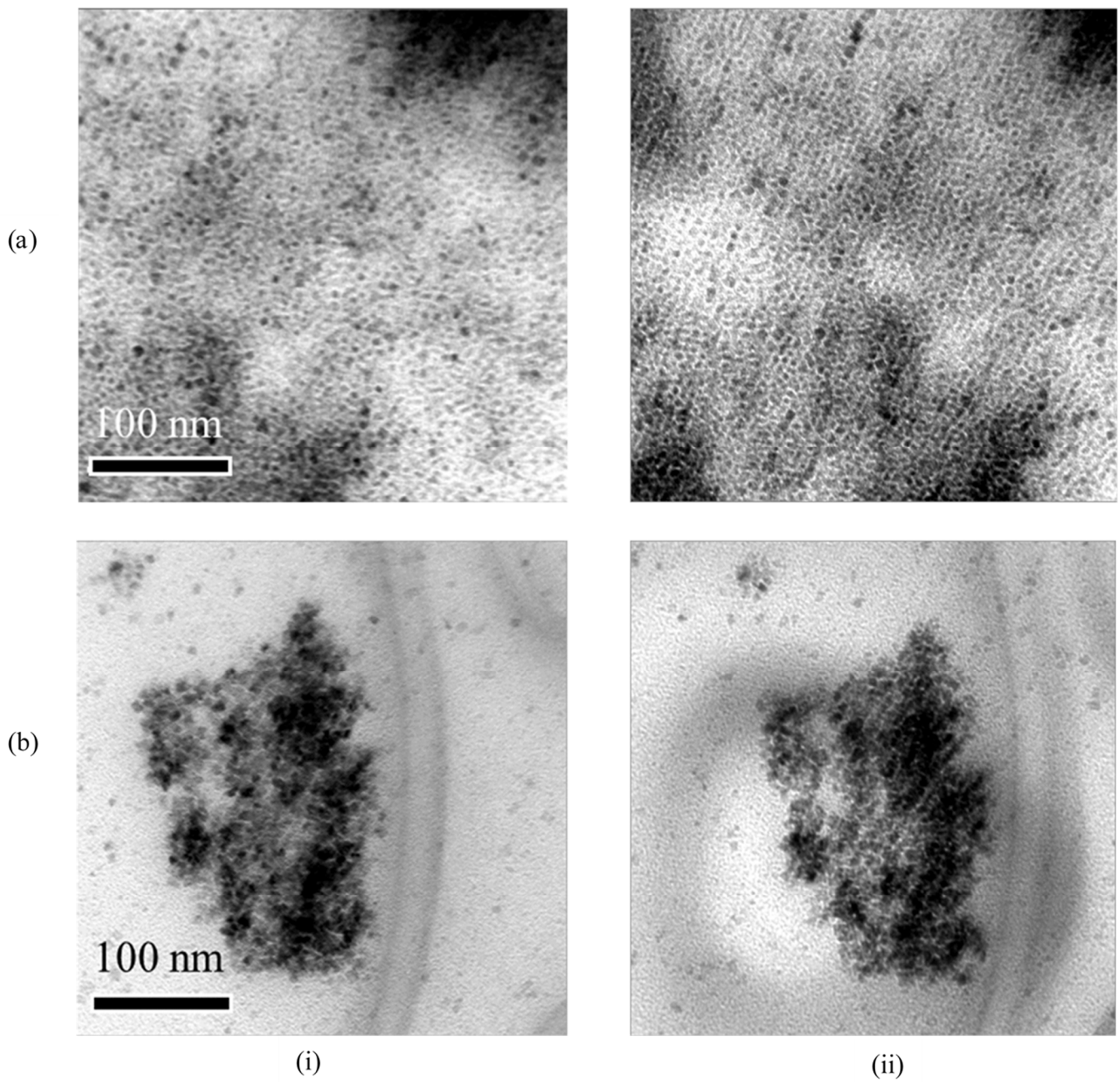


Figure 7. TEM images of nanoparticles generated from TBA preparation route during thermal annealing: (i) 25 °C and (ii) 500 °C where (a) CeO_x (scale bar = 100 nm) and (b) Eu:CeO_x (scale bar = 100 nm).

Table 2. Aerial density (μm^{-2}) and size (nm) versus temperature ($^{\circ}\text{C}$) for (a) ON, (b) HMTA, and (c) TBA preparation of CeO_2 and Eu:CeO_2 .

Prep Route	Temp ($^{\circ}\text{C}$)	Sample	Aerial Density (μm^{-2})	Size (nm)	Sample	Aerial Density (μm^{-2})	Size (nm)
ON	25	CeO_2	N/A	N/A	Eu:CeO_2	190.63	42.4
	100					201.06	42.34
	200					189.14	42.42
	300					177.23	42.42
	400					171.27	42.43
	500					160.85	42.45
HMTA	25	CeO_2	2919	5.77	Eu:CeO_2	2.204	340.57
	100		3216	5.75		2.204	340.61
	200		3797	5.79		2.204	340.6
	300		4932	5.84		2.204	340.59
	400		4676	5.81		2.204	340.6
	500		4649	5.81		2.204	340.62
TBA	25	CeO_2	15,882	4.07	Eu:CeO_2	4593	7.3
	100		16,445	4.04		4931	7.27
	200		15,519	4.09		5026	7.23
	300		15,501	4.09		4342	7.31
	400		14,818	4.1		3910	7.34
	500		14,083	4.12		3850	7.34

3.4. Irradiation Stability

The resistance of these nanoparticles to irradiation was evaluated by exposing the samples to different ion fluences. The TEM images of the ON, HDA, and TBA nanoparticles are shown in Figures 8–10, respectively.

For the $\text{CeO}_x(\text{ON})$ nanoparticles (see Figure 8i(a–c)), a decrease in crystallinity with increasing fluence was observed. This is consistent with the high concentration of defects that altered and/or destroyed the translational periodicity of the material. It was noted that at higher fluences, the ion irradiation also appeared to deplete the SiO_x layer beneath the nanoparticles, while simultaneously forcing the aggregation of the particle. By contrast, in the Eu-doped analog of Figure 8ii(a–c), remarkable radiation resistance was observed in the nanoparticles, with diffraction patterns (DP) revealing high crystallinity through the highest fluence studied. What appear to be ablation pits formed from sputtering events on the nanoparticle surface are easily visible. These surface defects are highlighted with arrows in Figure 8ii(c).

Figure 9i(a–c) shows the CeO_x (HMTA) preparation route. As can be observed, the polycrystalline green materials migrated towards a single crystalline/amorphous phase during exposure to various levels of ion irradiation. This process was likely akin to a recrystallization in the nanocubes with the simultaneous reduction in crystallinity at higher fluences. In Figure 9ii(a–c), the Eu-doped analog, it appears that the particles began to be sputtered at higher fluences, causing an overall reduction in the size of the nanoparticles. Additionally, the DP was amorphous where this process dominated the response of the material.

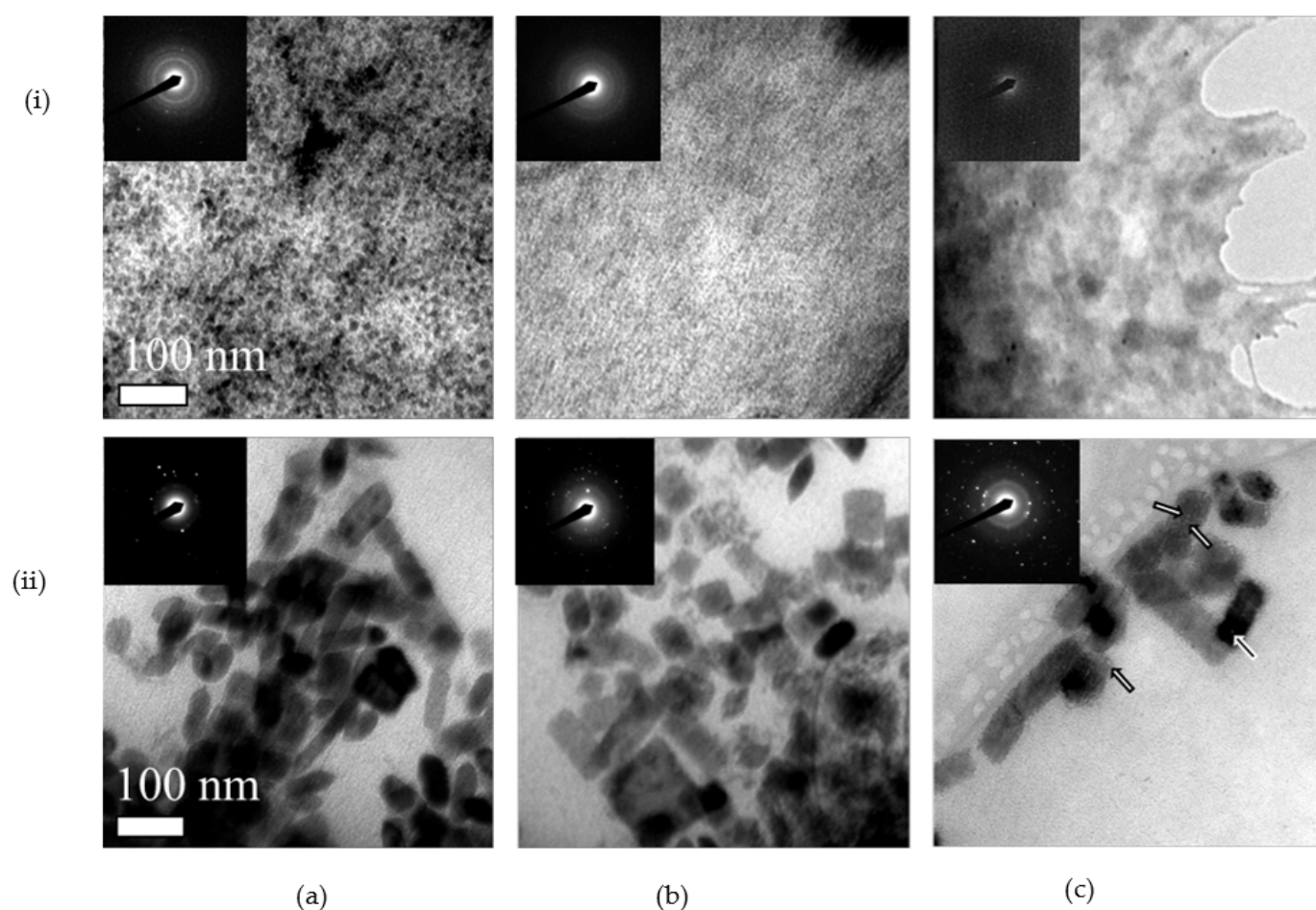


Figure 8. TEM images and SAED patterns of (i) CeO_x and (ii) Eu:CeO_x nanoparticles generated from ON preparation route during ion irradiation: (a) green, (b) $1 \times 10^{13} \text{ cm}^{-2}$, and (c) $1 \times 10^{15} \text{ cm}^{-2}$. Respective SAED patterns are displayed in the inset of each micrograph. Scale bars are 100 nm in all micrographs.

The $\text{CeO}_x(\text{TBA})$ nanoparticles, under the same ion exposure as that noted above, are shown in Figure 10i(a–c). As can be observed, the samples agglomerated as a result of destabilization from the ion interaction. This was further verified by the DP'S transition from a polycrystalline to an amorphous state. Lastly, in Figure 10ii(a–c), the Eu-doped particles remained separated at higher fluences and displayed a small amount of crystalline behavior at the highest fluence studied. These doped nanoparticle retained their structural integrity better than $\text{CeO}_x(\text{TBA})$ through ion irradiation.

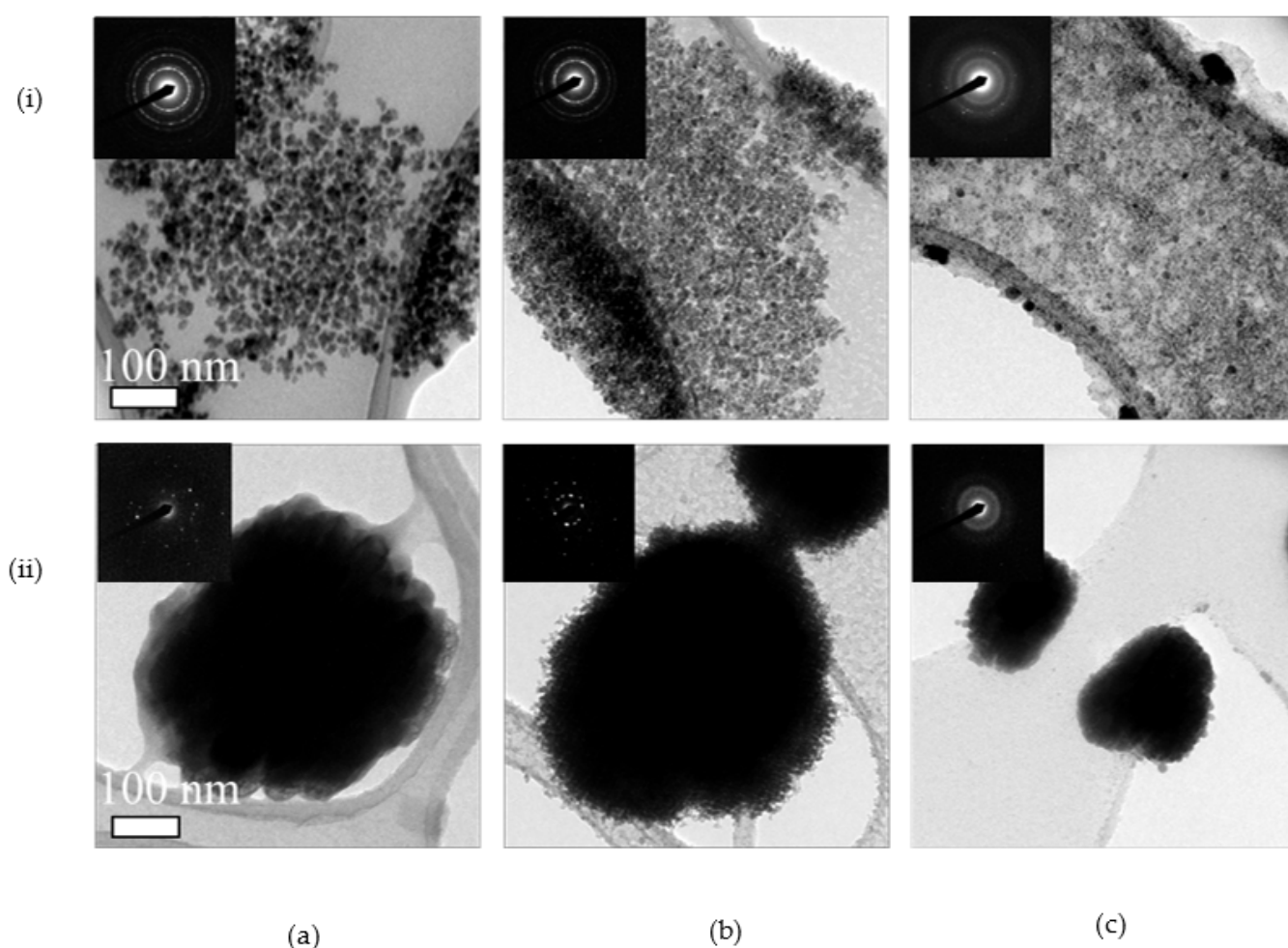


Figure 9. TEM images and SAED patterns of (i) CeO_x and (ii) Eu:CeO_x nanoparticles generated from HMTA preparation route during ion irradiation: (a) green, (b) $1 \times 10^{13} \text{ cm}^{-2}$, and (c) $1 \times 10^{15} \text{ cm}^{-2}$. Respective SAED patterns are displayed in the inset of each micrograph. Scale bars are 100 nm in all micrographs.

The high thermal stability of the particles was expected of these systems, given the high melting temperature (2400°C) of the CeO_x , which resulted in homologous temperatures of 0.21. Although well above the operating temperature of many applications, this temperature regime shows that no significant nanoscale-enhanced sintering is observed in these systems. The poor irradiation stability observed in this work is similar to that seen in crystalline tungstate nanoparticles irradiated with heavy ions [23,24]. This in stark contrast to other amorphous ceramic nanoparticles and core@shell nanoparticles that have been explored, which suggests that the amorphous phase may be extremely important for radiation stability [25,26]. As such, future work will explore the role of both phase and doping on the stability of ceramic nanoparticles for both free-standing nanoparticles, as shown in this study, as well as those embedded in composite matrixes.

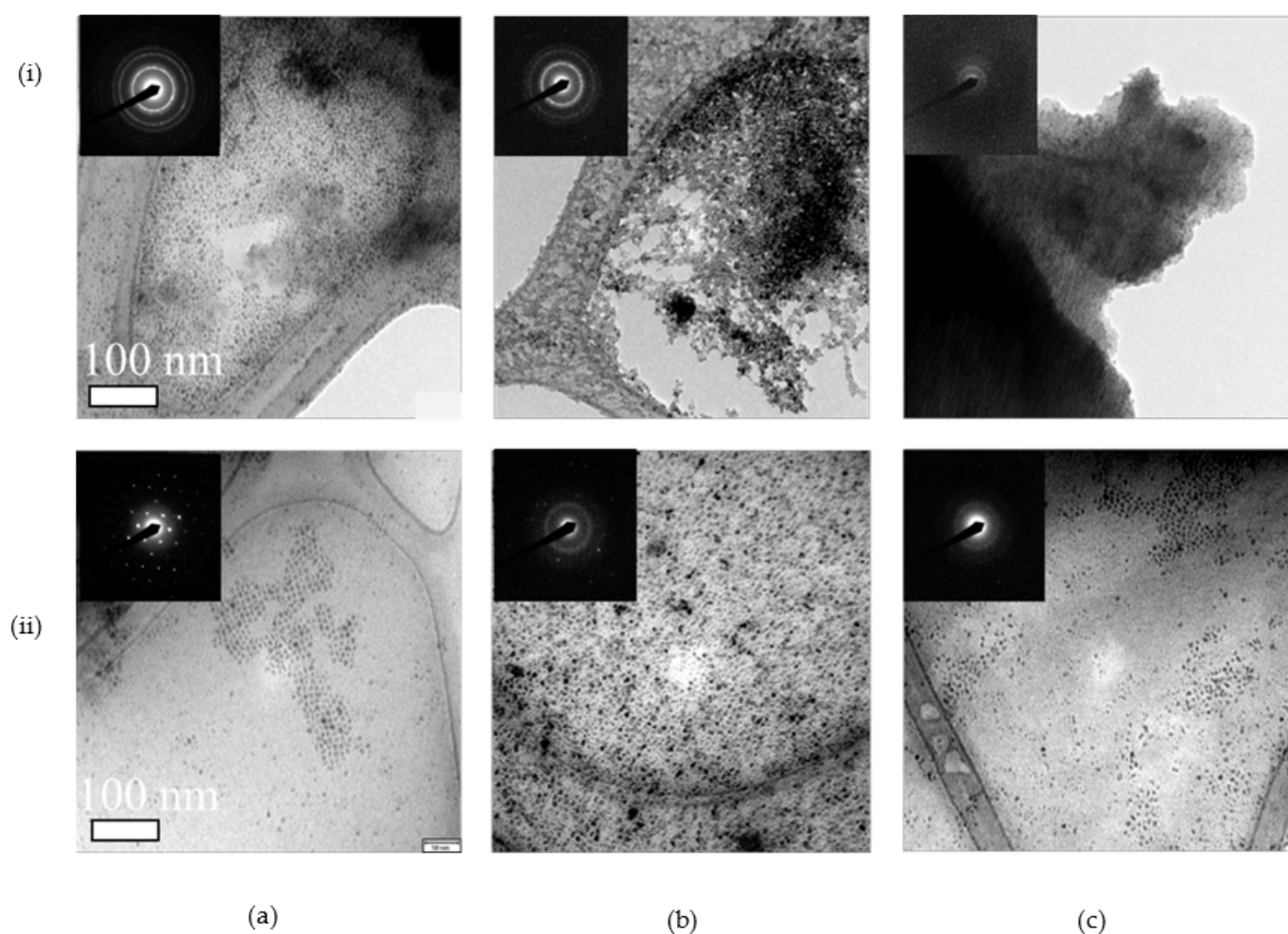


Figure 10. TEM images of (i) CeO_x and (ii) Eu:CeO_x nanoparticles generated from TBA preparation route during ion irradiation: (a) green, (b) $1 \times 10^{13} \text{ cm}^{-2}$, and (c) $1 \times 10^{15} \text{ cm}^{-2}$. Respective SAED patterns are displayed in the inset of each micrograph. Scale bars are 100 nm in all micrographs.

4. Summary and Conclusions

The synthesis of nanoparticles of CeO_x and Ln:CeO_x ($\text{Ln} = \text{Nd, Eu, Er, and Lu}$) was performed by using ON, HMTA, or TBA. The ON and TBA proved to be nanocubes whereas the HMTA produced larger rounded particulates. Elemental mapping and XRF studies confirmed the presence of the lanthanides, which were randomly distributed within a CeO_x matrix. Thermal analyses of the undoped and Eu-doped CeO_x samples for each preparative route revealed that the Ln-doped species appeared to be more resistant to thermal assaults in comparison to the undoped samples. In the ion stability studies, it was found that all of the samples displayed poor phase stability when exposed to 15 MeV Au ion irradiation. However, the Ln-doped species appeared to be slightly more stable than the homometallic nanoparticles. This variation suggests a potential difference in the active microstructural mechanisms during thermal annealing and ion irradiation. These results suggest that doping with alternative lanthanide cations in CeO_x could serve as a good shielding agent against external stimuli.

Supplementary Materials: The following are available online at <https://www.mdpi.com/article/10.3390/cryst11111369/s1>. Figure S1: Analytical data for generated CeO_x (a) XRF [(i) ON, (ii) HMTA, (iii) TBA], (b) pXRD RT [(i) ON, (ii) HMTA, (iii) TBA], (b*) pXRD 600 °C [(i) ON, (ii) HMTA, (iii) TBA], (c) FTIR [(i) ON, (ii) HMTA, (iii) TBA], (d) DLS [(i) ON, (ii) HMTA, (iii) TBA], (e) TGA/DSC [(i) ON, (ii) HMTA, (iii) TBA]; Figure S2: Analytical data for generated Nd:CeO_x (a) XRF [(i) ON, (ii) HMTA,

(iii) TBA], (b) pXRD RT [(i) ON, (ii) HMTA, (iii) TBA], (b*) pXRD 600 °C [(i) ON, (ii) HMTA, (iii) TBA], (c) FTIR [(i) ON, (ii) HMTA, (iii) TBA], (d) DLS [(i) ON, (ii) HMTA, (iii) TBA]; Figure S3: Analytical data for generated Eu:CeO_x (a) XRF [(i) ON, (ii) HMTA, (iii) TBA], (b) pXRD RT [(i) ON, (ii) HMTA, (iii) TBA], (b*) pXRD 600 °C [(i) ON, (ii) HMTA, (iii) TBA], (c) FTIR [(i) ON, (ii) HMTA, (iii) TBA], (d) DLS [(i) ON, (ii) HMTA, (iii) TBA], (e) TGA/DSC [(i) ON, (ii) HMTA, (iii) TBA]; Figure S4: Analytical data for generated Er:CeO_x (a) XRF [(i) ON, (ii) HMTA, (iii) TBA], (b) pXRD RT [(i) ON, (ii) HMTA, (iii) TBA], (b*) pXRD 600 °C [(i) ON, (ii) HMTA, (iii) TBA], (c) FTIR [(i) ON, (ii) HMTA, (iii) TBA], (d) DLS [(i) ON, (ii) HMTA, (iii) TBA]; Figure S5: Analytical data for generated Lu:CeO_x (a) XRF [(i) ON, (ii) HMTA, (iii) TBA], (b) pXRD RT [(i) ON, (ii) HMTA, (iii) TBA], (b*) pXRD 600 °C [(i) ON, (ii) HMTA, (iii) TBA], (c) FTIR [(i) ON, (ii) HMTA, (iii) TBA], (d) DLS [(i) ON, (ii) HMTA, (iii) TBA].

Author Contributions: Conceptualization, T.J.B. and K.H.; methodology, T.J.B., K.H. and K.B.; software, K.B.; validation, T.J.B. and K.H.; formal analysis, T.J.B., K.H., K.B., P.C.R. and F.G.; investigation, T.J.B.; resources, T.J.B., K.H. and P.L.; data curation, K.B., P.C.R., F.G. and P.L.; writing—original draft preparation, T.J.B. and K.B.; writing—review and editing, T.J.B., K.H., K.B., P.C.R., F.G., E.L., P.L. and A.A.; visualization, K.B. and P.C.R.; supervision, T.J.B. and K.H.; project administration, T.J.B. and K.H.; funding acquisition, T.J.B. and K.H. All authors have read and agreed to the published version of the manuscript.

Funding: This work was supported by Sandia National Laboratories.

Data Availability Statement: Not applicable.

Acknowledgments: This work was performed, in part, at the Center for Integrated Nanotechnologies, an Office of Science User Facility operated for the U.S. Department of Energy (DOE) Office of Science. Sandia National Laboratories is a multimission laboratory managed and operated by National Technology & Engineering Solutions of Sandia, LLC, a wholly owned subsidiary of Honeywell International, Inc., for the U.S. DOE's National Nuclear Security Administration under contract DE-NA-0003525. The views expressed in the article do not necessarily represent the views of the U.S. DOE or the United States Government.

Conflicts of Interest: The authors declare no conflict of interest.

References

- Baker, C.H. Harnessing cerium oxide nanoparticles to protect normal tissue from radiation damage. *Transl. Cancer Res.* **2013**, *2*, 343–358.
- Issa, S.A.M.; Sayyed, N.I.; Zaid, N.H.N.; Matori, K.A. Effect of Bi₂O₃ in borate-tellurite-silicate glass system for development of gamma-rays shielding materials. *Results Phys.* **2018**, *9*, 206–210. [\[CrossRef\]](#)
- Niranjan, R.S.; Rudraswamy, B.; Dhananjaya, N. Effective atomic number, electron density and kerma of gamma radiation for oxides of lanthanides. *Pramana* **2012**, *78*, 451–458. [\[CrossRef\]](#)
- Al-Hadeethia, Y.; Sayyed, M.I.; Kaewkhao, J.; Raffah, B.M.; Almalkia, R.; Rajaramakrishnad, R.; Hussein, M.A. Chalcogenide glass-ceramics for radiation shielding applications. *Ceram. Int.* **2020**, *46*, 5380–5386.
- Abd-Allah, W.M.; Fayad, A.M.; Saudi, H.A. Structure and Physical Properties of Al₂O₃ Nanofillers Embedded in Poly(Vinyl Alcohol). *Opt. Quantum Electron.* **2019**, *51*, 1–14.
- Graham, J.T.; Zhang, Y.; Weber, W.J. Irradiation-induced defect formation and damage accumulation in single crystal CeO₂. *J. Nucl. Mater.* **2018**, *498*, 400–408. [\[CrossRef\]](#)
- Costantini, J.M.; Lelong, G.; Guillaumet, M.; Gourier, D. Recovery of damage in electron-irradiated ceria. *J. Appl. Phys.* **2021**, *129*, 155901. [\[CrossRef\]](#)
- Sorenson, J.J.; Tieu, E.; Morse, M.D. Bond dissociation energies of lanthanide sulfides and selenides. *J. Chem. Phys.* **2021**, *154*, 124307. [\[CrossRef\]](#)
- Dhall, A.; Self, W. Cerium Oxide Nanoparticles: A Brief Review of Their Synthesis Methods and Biomedical Applications. *Antioxidants* **2018**, *7*, 97. [\[CrossRef\]](#)
- Xu, C.; Qu, X. Cerium oxide nanoparticle: A remarkably versatile rare earth nanomaterial for biological applications. *NPG Asia Mater.* **2014**, *6*, e90. [\[CrossRef\]](#)
- Wang, G.; Peng, Q.; Li, Y. Lanthanide-Doped Nanocrystals: Synthesis, Optical-Magnetic Properties, and Applications. *Accounts Chem. Res.* **2010**, *44*, 322–332. [\[CrossRef\]](#)
- Wang, Z.; Quan, Z.; Lin, J. Remarkable Changes in the Optical Properties of CeO₂ Nanocrystals Induced by Lanthanide Ions Doping. *Inorg. Chem.* **2007**, *46*, 5237–5242. [\[CrossRef\]](#) [\[PubMed\]](#)
- Lin, Y.-H.; Shen, L.-J.; Chou, T.-H.; Shih, Y.-H. Synthesis, Stability, and Cytotoxicity of Novel Cerium Oxide Nanoparticles for Biomedical Applications. *J. Clust. Sci.* **2021**, *32*, 405–413. [\[CrossRef\]](#)

14. Kumar, A.; Babu, S.; Karakoti, A.S.; Schulte, A.; Seal, S. Luminescence Properties of Europium-Doped Cerium Oxide Nanoparticles: Role of Vacancy and Oxidation States. *Langmuir* **2009**, *25*, 10998–11007. [[CrossRef](#)] [[PubMed](#)]
15. Hubbard, J.A.; Boyle, T.J.; Sepper, E.T.; Brown, A.; Settecerci, T.; Santaripa, J.L.; Kotula, P.; McKenzie, B.; Lucero, G.A.; Lemieux, L.J.; et al. Airborne Release Fractions from Surrogate Nuclear Waste Fires Containing Lanthanide Nitrates and Depleted Uranium Nitrate in 30% Tributyl Phosphate in Kerosene. *Nucl. Technol.* **2021**, *207*, 103–118. [[CrossRef](#)]
16. Olegário, R.C.; de Souza, E.C.F.; Borges, J.F.M.; da Cunha, J.B.M.; de Andrade, A.V.C.; Antunes, S.R.M.; Antunes, C.A. Synthesis and characterization of Fe³⁺ doped cerium–praseodymium oxide pigments. *Dye. Pigment.* **2013**, *97*, 113–117. [[CrossRef](#)]
17. Yabe, S.; Yamashita, M.; Momose, S.; Tahira, K.; Yoshida, S.; Li, R.; Yin, S.; Sato, T. Synthesis and UV-shielding properties of metal oxide doped ceria via soft solution chemical processes. *Int. J. Inorg. Mater.* **2001**, *3*, 1003–1008. [[CrossRef](#)]
18. Cabral, A.C.; Cavalcante, L.S.; Deus, R.C.; Longo, E.; Simoes, A.Z.; Moura, F. Photoluminescence properties of praseodymium doped cerium oxide nanocrystals. *Ceram. Int.* **2014**, *40*, 4445–4453. [[CrossRef](#)]
19. Hattar, K.; Bufford, D.C.; Buller, D.L. Concurrent in situ ion irradiation transmission electron microscope. *Nucl. Instrum. Methods Phys. Res. Sect. B Beam Interact. Mater. At.* **2014**, *338*, 56–65. [[CrossRef](#)]
20. Yu, T.; Park, Y.I.; Kang, M.-C.; Joo, J.; Par, J.K.; Won, H.Y.; Hyeon, K.J.J.T. Large-Scale Synthesis of Water Dispersible Ceria Nanocrystals by a Simple Sol–Gel Process and Their Use as a Chemical Mechanical Planarization Slurry. *Eur. J. Inorg. Chem.* **2008**, *2008*, 855–858. [[CrossRef](#)]
21. Zhang, F.; Chan, S.-W.; Spanier, J.E.; Apak, E.; Jin, Q.; Robinson, R.D.; Herman, I.P. Cerium oxide nanoparticles: Size-selective formation and structure analysis. *Appl. Phys. Lett.* **2002**, *80*, 127–129. [[CrossRef](#)]
22. Yang, S.; Gao, L. Controlled Synthesis and Self-Assembly of CeO₂ Nanocubes. *J. Am. Chem. Soc.* **2006**, *128*, 9330–9331. [[CrossRef](#)] [[PubMed](#)]
23. Branson, J.V.; Hattar, K.; Rossi, P.; Vizkelethy, G.; Powell, C.J.; Hernandez-Sanchez, B.; Doyle, B. Ion beam characterization of advanced luminescent materials for application in radiation effects microscopy. *Nucl. Instrum. Methods Phys. Res. Sect. B Beam Interact. Mater. At.* **2011**, *269*, 2326–2329. [[CrossRef](#)]
24. Hoppe, S.M.; Hattar, K.; Boyle, T.J.; Villone, J.; Yang, P.; Patrick Doty, F.; Hernandez-Sanchez, B.A. Application of in-situ ion irradiation TEM and 4D tomography to advanced scintillator materials. In *Penetrating Radiation Systems and Applications XIII*; International Society for Optics and Photonics: Bellingham, WA, USA, 2012; Volume 8509.
25. Blair, S.J.; Muntifer, B.R.; Chan, R.O.; Barr, C.M.; Boyle, T.J.; Hattar, K. Unexpected radiation resistance of core/shell ceramic oxide nanoparticles. *Mater. Today Commun.* **2018**, *17*, 109–113. [[CrossRef](#)]
26. Kiani, M.T.; Hattar, K.; Wendy Gu, X. In situ TEM Study of Radiation Resistance of Metallic Glass–Metal Core–Shell Nanocubes. *ACS Appl. Mater. Interfaces* **2020**, *12*, 40910–40916. [[CrossRef](#)] [[PubMed](#)]